JOURNAL OF PETROLOGY | VOLUME 50 | NUMBER 7 | PAGES 1359–1375 | 2009 | doi:10.1093/petrology/egn082

Sr–Nd–Pb–He–O Isotope and Geochemical Constraints on the Genesis of Cenozoic Magmas from the West Antarctic Rift

ISABELLA NARDINI[1]*, PIETRO ARMIENTI[2], SERGIO ROCCHI[2], LUIGI DALLAI[3] AND DARRELL HARRISON[4]

[1]DIPARTIMENTO DI SCIENZE DELLA TERRA, UNIVERSITÀ DI PISA, 56126 PISA, ITALY; ISTITUTO DI GEOSCIENZE E GEORISORSE (IGG-CNR), VIA MORUZZI 1, 56124 PISA, ITALY

[2]DIPARTIMENTO DI SCIENZE DELLA TERRA, UNIVERSITÀ DI PISA, 56126 PISA, ITALY

[3]ISTITUTO DI GEOSCIENZE E GEORISORSE (IGG-CNR), 56124 PISA, ITALY

[4]SCHOOL OF EARTH, ATMOSPHERIC AND ENVIRONMENTAL SCIENCES, UNIVERSITY OF MANCHESTER, OXFORD ROAD, MANCHESTER M13 9PL, UK

RECEIVED MAY 21, 2008; ACCEPTED DECEMBER 24, 2008
ADVANCE ACCESS PUBLICATION JANUARY 22, 2009

The West Antarctic Rift System (WARS) represents one of the major active continental extension zones on Earth. The Ross Sea coast in northern Victoria Land (NVL) is littered with alkaline rift-related igneous products (Middle Eocene–Present). This study characterizes the nature of the magma source involved in the rift process through geochemical–isotopic investigation of Cenozoic basalts from NVL, and provides important constraints for the reconstruction of the tectono-magmatic evolution of the Ross Sea region–WARS. The chemical compositions of the basalts (Miocene–Present) display major and trace element characteristics typical of ocean island basalts (OIB), with strong enrichment in the most incompatible elements. Whole-rock isotopic compositions are in the range 0·7028–0·7034 for $^{87}Sr/^{86}Sr$, 0·5129–0·5130 for $^{143}Nd/^{144}Nd$ ($\varepsilon_{Nd(t)} \sim$ 4·8–6·7), 19·3–19·7 for $^{206}Pb/^{204}Pb$, 15·4–15·6 for $^{207}Pb/^{204}Pb$ and 38·7–39·3 for $^{208}Pb/^{204}Pb$, suggesting a HIMU-like (high U/Pb) signature of the mantle source. Determinations of $^{3}He/^{4}He$ on crushed olivine yielded values between 5·7 and 7·2 times the atmospheric ratio, similar to the lithospheric mantle and in the range of mid-ocean ridge basalts (MORB). The $\delta^{18}O_{ol}$ of olivine separates varies from 4·92 to 5·53‰ and is positively correlated with Fo content. Integration of our geochemical and isotope data with available geological, geophysical and geochronological data has led to the following reconstruction. The differences in the oxygen isotope values principally reflect the involvement of a heterogeneous mantle source and/or the assimilation of variable amounts of hydrothermally altered crustal rocks from the volcanic edifices. The $^{3}He/^{4}He$ data allow us to exclude a plume-driven model to explain the continuing rifting process. Based on the evidence of metasomatic processes, we propose a model to generate the mantle source(s) of the Cenozoic basaltic melts of the NVL. This is sublithospheric mantle metasomatized during an amagmatic extensional event that affected the WARS in the Late Cretaceous. During Eocene–Oligocene times, mantle flow warmed the mantle at the edge of the thick Antarctic lithosphere, and the reactivation of old translithospheric discontinuities promoted mantle melting and the rise of magmas as plutons and dyke swarms. From the Late Miocene to Present, the continuing craton-directed mantle flow led to normal faulting of the rift shoulder, which favoured the rise of magmas to build up large volcanic edifices.

KEY WORDS: *Antarctica; geochemistry; Sr–Nd–Pb–He–O isotopes; lithospheric mantle; metasomatism*

INTRODUCTION

Studies on the evolution of continental rift systems and rifted continental margins have led to the development of

*Corresponding author. Present address: Istituto di Geoscienze e Georisorse (IGG-CNR), Via Moruzzi 1, 56124 Pisa, Italy. Telephone: +39 050 3153410. Fax: +39 050 3869104.
E-mail: nardini@igg.cnr.it

many hypotheses about their origin. A classic element of controversy is whether rift zones are produced by actively upwelling mantle splitting the continent, possibly along pre-weakened zones, or whether the mantle rises passively as the continents are pulled apart during lithospheric stretching. A major line of evidence used to solve this question is commonly provided by the geochemical and isotopic compositions of rift-related igneous products. This line of investigation is framed in the overall discussion of the origin of alkaline lavas in intraplate settings, either continental or oceanic.

In the past 20 years, a wealth of new geological, geophysical, geochemical and geochronological data has shown that the West Antarctic Rift System (WARS) is one of the most important intracontinental rifts on Earth. The Middle Eocene to Present alkaline magmatism of the WARS has been interpreted in terms of different types of rift activity. Several papers have invoked the occurrence of an active plume centred below either Marie Byrd Land or Victoria Land–Mt. Erebus (LeMasurier & Rex, 1989; Behrendt *et al.*, 1991; Hole & LeMasurier, 1994; LeMasurier & Landis, 1996; Storey *et al.*, 1999). This hypothesis is based on: (1) the similar geochemical characteristics of basalts from the WARS and ocean island basalts (OIB) associated with long-lived hotspot tracks; (2) the occurrence of an uplifted dome in Marie Byrd Land accompanied by horst–graben sub-ice topography; (3) the modest Cenozoic extension with respect to the large volume of observed Cenozoic magmatism; (4) the inferred lack of tectonic events coeval within rifting and volcanism in West Antarctica; (5) the high heat flow in the Ross Sea area. On the basis of the geochemical characteristics of the magmatic rocks, this model has been progressively extended to various parts of the rift.

Other studies favour a passive model in which the source for all the HIMU volcanism in the SW Pacific can be related to a 'fossil' plume head fixed at the base of the lithosphere prior to the mid-Cretaceous break-up of New Zealand from Antarctica (Rocholl *et al.*, 1995; Hart *et al.*, 1997; Panter *et al.*, 2000).

Alternative interpretations to both plume-driven and passive rifting have been proposed by Rocchi *et al.* (2002, 2003, 2005), which suggest that magma genesis and emplacement is due to the reactivation of pre-existing NW–SE translithospheric faults (Salvini *et al.*, 1997), which promoted local decompression melting of an enriched mantle previously veined during a Late Cretaceous amagmatic extensional rift phase. This hypothesis was developed by integrating structural, geochronological and geochemical observations such as the following: (1) the dominance of Cenozoic geodynamics by intraplate right-lateral strike-slip tectonics, which induced a significant oblique component to the rifting process; (2) the geometric link of the rift-related magmatism to the interplay between NW–SE Palaeozoic faults (linked with the major transform faults in the Southern Ocean) and north–south late Cretaceous extensional faults; (3) the absence of doming on the western coast of the Ross Sea, and rather, the presence of a linear surface uplift dissected by transverse fault systems in northern Victoria Land (NVL); (4) the occurrence of the main extensional episode during the Late Cretaceous, and the beginning of the main denudation–uplift event in the Middle Eocene, coeval with the onset of magmatic activity.

Another model, proposed by Finn *et al.* (2005), suggests that swift detachment and sinking of Palaeozoic–Mesozoic (~500–100 Ma) subducted slabs in the Late Cretaceous induced instabilities along the former Gondwana margin that triggered lateral and vertical flow of warm Pacific mantle. The interaction between the warm mantle and the metasomatized subcontinental lithosphere of the SW Pacific magmatic province would have concentrated magmatism along zones of weakness. In particular, Panter *et al.* (2006) have suggested that the mantle sources of the alkaline magmatism represent continental lithosphere that hosted amphibole- or phlogopite-rich veins formed by plume- and/or subduction-related metasomatism between 500 and 100 Ma.

This study characterizes the mantle source(s) involved in the WARS igneous province through geochemical and isotopic studies of Cenozoic basalts from NVL, and focuses on the reconstruction of the links between the WARS–Southern Ocean evolution and the development of the source-melt system of the western Ross Sea area.

THE WEST ANTARCTIC RIFT SYSTEM

The WARS (Fig. 1) is bordered on the west by a high-standing rift flank, the Transantarctic Mountains (TAM). Geophysical data indicate a crustal thickness of the order of 40 km beneath the TAM, which rapidly decreases to 25 km beneath the coast of the Ross Sea and reaches a minimum of about 18 km in the Victoria Land Basin (Della Vedova *et al.*, 1997).

Since the Middle Eocene, the WARS was affected by widespread alkaline igneous activity in northern Vicoria Land, mainly developed at the intersection of NW–SE and north–south extensional faults (Salvini *et al.*, 1997). Plutons and dyke swarms, collectively named the Meander Intrusive Group (Müller *et al.*, 1991; Tonarini *et al.*, 1997), and volcanic products of the McMurdo Volcanic Group (MMVG; Harrington, 1958) are exposed in the coastal area of Victoria Land. Plutons crop out

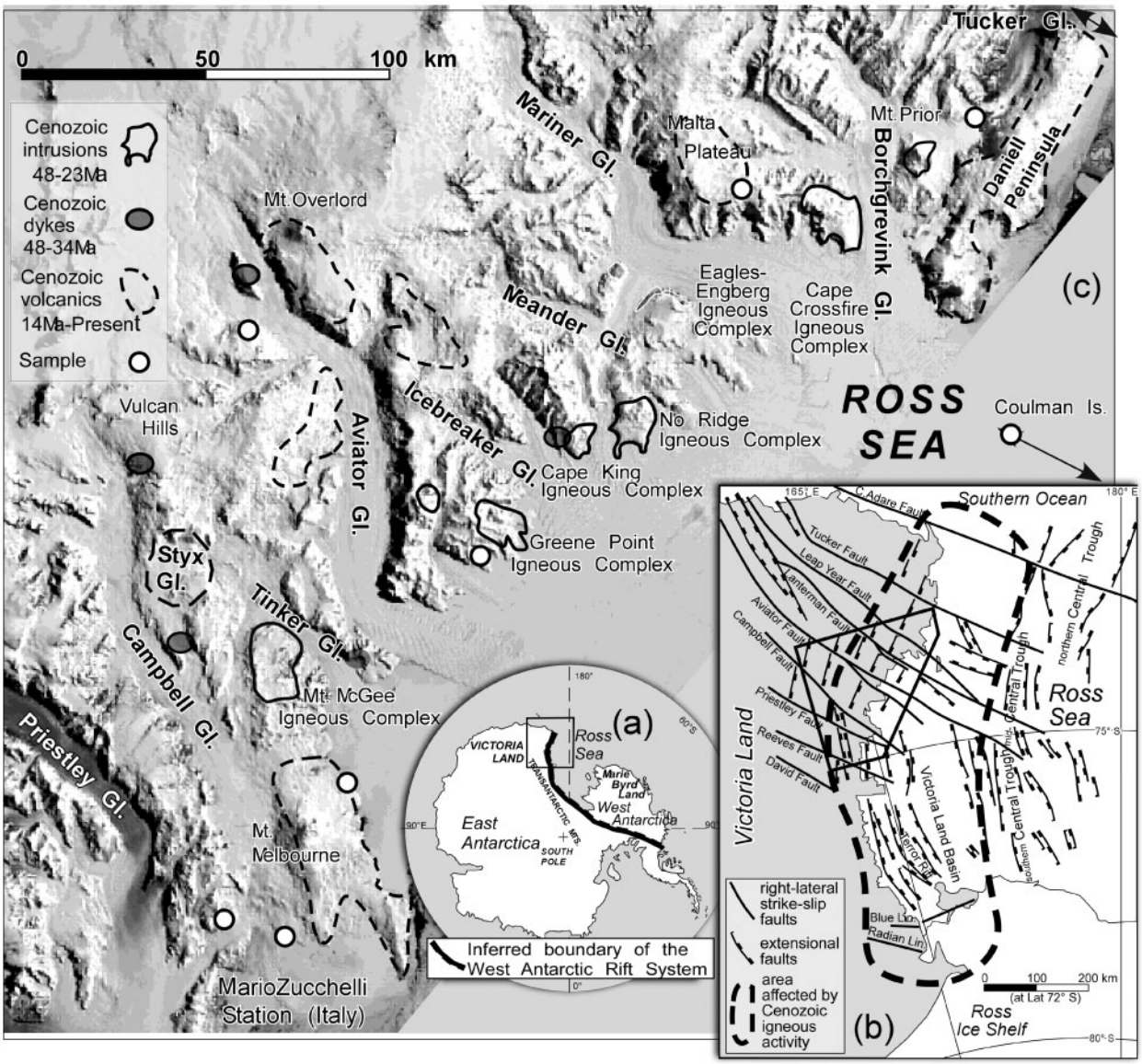

Fig. 1. (a) Map of Antarctica showing the approximate boundaries of the WARS. The rectangle represents the area shown in (b). (b) Structural tectonic map of the western Ross Embayment, including Victoria Land and the western Ross Sea area (Salvini *et al.*, 1997; Salvini & Storti, 1999; Rocchi *et al.*, 2002). Tectonic lineaments in southern Victoria Land after Wilson (1999). The irregular box represents the area shown in (c). (c) Outcrops of the Cenozoic magmatic products and location of the sampled lavas (it should be noted that Coulman Island is outside the area of the satellite image). Base image is a Landsat satellite image mosaic in Lambert conformal conic projection, courtesy of Lucchitta *et al.* (1987).

in a 200 km long section of the western rift shoulder (between the Campbell and Leap Year Faults), and are usually associated with strong positive magnetic anomalies (Müller *et al.*, 1991). Their age is between 48 and 23 Ma (Müller *et al.*, 1991; Tonarini *et al.*, 1997). Dykes occur over a widespread area and crosscut both Palaeozoic basement and Cenozoic igneous complexes over a time span of 48–34 Ma (Tonarini *et al.*, 1997; Rocchi *et al.*, 2002). Volcanic edifices that can be recognized within the MMVG are basaltic shield volcanoes, stratovolcanoes with dominant trachytic and phonolitic compositions, and small, isolated basaltic scoria cones and lava flows. Plutonic and volcanic activities represent, respectively, the earliest (45–23 Ma) and the latest (19–0 Ma) (Armienti & Baroni, 1999) records of regionally extensive rift-related magmatic activity.

WHOLE-ROCK DATA

Petrography and trace element geochemistry

Samples were collected on the Ross Sea coast, between the Tucker and Priestley glaciers and on Coulman Island, from monogenetic scoria cones where small lava flows often occurred at the end of the explosive activity (Fig. 1).

Textures vary from sub-aphyric to weakly porphyritic. Olivine is generally the only phenocryst phase, thus representing the first liquidus phase, although some of the samples show also minor amounts of augitic clinopyroxene phenocrysts and sporadic olivine and orthopyroxene xenocrysts. Olivine phenocrysts are usually euhedral with polygonal habit and frequently contain subhedral to euhedral spinel inclusions and rare multiphase melt inclusions (Orlando *et al.*, 1997). Microphenocrysts are represented by unzoned clinopyroxene and euhedral olivine. The groundmasses vary from microcrystalline to cryptocrystalline and are composed of clinopyroxene, opaque minerals, plagioclase and sometimes olivine. Interstitial nepheline often occurs in the most crystalline varieties. Apatite is a common accessory phase in all the studied rocks. Olivine and orthopyroxene xenocrysts are usually rounded in shape, and their size is usually larger than that of phenocrysts. Olivine xenocrysts always display kink banding whereas orthopyroxene xenocrysts are mantled by coronas of clinopyroxene and sometimes olivine.

Major and trace elements analyses are reported in Table 1. The selected lavas are basanites and basalts, with the exception of one sample (SAX20), which is an olivine nephelinite. In the total alkalis vs silica classification diagram, they plot within the alkaline field (Fig. 2). The SiO_2 content is in the range of 41–46 wt %, with K_2O/Na_2O values from 0·29 to 0·44 revealing a distinct sodic affinity (Fig. 2). The overall set of samples has $59{\cdot}3 <$ Mg-number $< 71{\cdot}8$ [Mg-number $= 100\ Mg/(Mg + Fe^{2+})$]. Cr contents range from 360 to 713 ppm. According to their CIPW norms, all the rocks are *ne*-normative, except for one, which is *hy*-normative (sample MB65b; Table 1). Variations in incompatible element ratios are very small; for example, La/Nb (<0·80) and Ba/Nb do not vary with magnesium content (MgO ~8–12 wt %). The chondrite-normalized distribution of the rare earth elements (REE) in the lavas (Fig. 3) shows similar patterns for all the samples, with significant light REE (LREE) enrichment (La_N ~120–180) with respect to chondritic values. The Eu anomaly is absent or slightly positive (Eu/Eu^* ~0·95–1·06) without evidence of cumulus plagioclase. All the patterns are very similar, with the exception of the olivine nephelinite (SAX20), which is extremely enriched in REE (La_N ~530). The multi-element patterns normalized to the Primordial Mantle composition (Fig. 4) reveal high ratios of Nb–Ta to large ion lithophile elements (LILE; Ce, Rb, K, Ba, Sr, Eu) and high primitive mantle-normalized La/K. The negative anomalies of K and Pb are prominent and occur in all samples. Sample SAX20 is the most enriched in incompatible elements and, consequently, shows the most prominent negative K anomaly.

Sr, Nd and Pb isotope ratios

Analysed samples from NVL have relatively low $^{87}Sr/^{86}Sr$, moderately high $^{143}Nd/^{144}Nd$ and high $^{206}Pb/^{204}Pb$ isotopic values (Table 2). Isotopic compositions are in the range of 0·7028–0·7034 for $^{87}Sr/^{86}Sr$, 0·51288–0·51298 for $^{143}Nd/^{144}Nd$ (corresponding to $\varepsilon_{Nd(t=0)}$ ~4·8–6·7), 19·3–19·7 for $^{206}Pb/^{204}Pb$, 15·4–15·6 for $^{207}Pb/^{204}Pb$ and 38·7–39·3 for $^{208}Pb/^{204}Pb$. In Figs 5 and 6 the data are compared with the mantle end-members of Zindler & Hart (1986) and with other OIB occurrences according to their geographical location. Figure 5 shows the $\varepsilon_{Nd(t=0)}$–$^{87}Sr/^{86}Sr$ correlation diagram. The samples plot in the depleted quadrant of the diagram and display a negative correlation. The $^{206}Pb/^{204}Pb$ isotope ratios are fairly similar when compared with the relatively variable $^{87}Sr/^{86}Sr$ and $^{143}Nd/^{144}Nd$ values (Fig. 6a and b). The most radiogenic Nd isotope composition is displayed by sample SAX20.

OLIVINE DATA

Chemistry

Petrographic and geochemical data combined with published experimental work (Orlando *et al.*, 1997, 2000; Perinelli *et al.*, 2006) for the studied lavas suggests that they are relatively primitive. For this reason the study of olivine phenocrysts is particularly suited to give geochemical and thermal information about the mantle source region.

The olivine grains are 0·5–2·0 mm in size and have a pale green body colour. Their forsterite contents are in the range of $Fo_{92–66}$ (Table 3), indicating different degrees of evolution of the melt from which they crystallized. Zoning is weak or absent. Ni and Cr are above the detection limit, as expected in Mg-rich olivine; chromium usually occurs in minute exsolved lamellae of chromite. Olivines with CaO contents lower than 0·10 wt % and with very high Fo (90–80 mol %) (Fig. 7) overlap the composition of olivine from peridotite xenoliths from Mt. Melbourne (Zipfel & Wörner, 1992). On the basis of more than 145 electron microprobe analyses, most of the olivine compositions (MgO and CaO) are in equilibrium with those of the whole-rocks (Roeder & Emslie, 1970; Jurewicz & Watson, 1988); some of the olivine from samples SAX20 and MB33 is clearly derived from mantle xenoliths, which show pronounced kink-banding and irregular shapes typical of disequilibrium crystals. Microthermometric experiments on primary melt inclusions hosted by olivine (samples MB33, MP34, MP24) gave homogenization

Table 1: Data sources for major elements

Location:	Greene Point	Coulman Island	Malta Plateau	Coulman Island	Browning Pass	Baker Rocks	Daniell Peninsula	Shield Nunatak	Baker Rocks	Shield Nunatak	Baker Rocks	Nathan Hills
Sample:	SAX20	MP34	MP24	MP32	MB65b	MB54	MP8	MB27	MB32	MB26	MB33	MB78
Major elements (wt %)												
SiO_2	40·78	42·81	43·31	43·88	43·91	44·09	44·12	44·16	44·68	44·76	45·67	45·84
TiO_2	3·62	3·08	2·80	3·39	2·76	3·01	2·71	2·99	3·16	2·97	2·81	2·24
Al_2O_3	11·81	14·79	13·87	15·71	14·30	13·92	14·87	14·89	15·11	14·30	15·31	16·72
Fe_2O_3	11·00	3·19	2·68	4·02	4·30	2·12	5·06	2·54	2·87	1·69	2·04	2·06
FeO	4·60	8·80	7·94	8·32	8·49	9·89	8·20	9·29	9·15	9·97	9·37	9·18
MnO	0·28	0·19	0·18	0·20	0·20	0·19	0·20	0·18	0·17	0·19	0·17	0·19
MgO	9·33	11·14	12·50	8·36	10·30	12·03	9·51	9·45	10·31	10·18	10·21	8·25
CaO	9·23	10·99	11·03	10·42	9·04	9·27	10·89	11·57	8·97	11·44	8·52	9·67
Na_2O	5·31	2·80	2·99	3·33	2·85	2·88	2·52	2·49	3·25	2·63	3·58	3·41
K_2O	1·54	1·03	1·31	1·11	1·11	1·17	0·79	0·76	1·16	0·75	1·25	1·14
P_2O_5	1·60	0·60	0·56	0·67	0·53	0·51	0·39	0·64	0·50	0·59	0·52	0·41
LOI	0·90	0·58	0·84	0·60	2·20	0·93	0·73	1·04	0·68	0·54	0·56	0·89
Total	100·00	100·00	100·00	100·01	99·99	100·01	100·00	100·00	100·01	100·01	100·01	100·00
Mg-no.	59·3	66·7	71·8	59·6	63·7	68·2	61·1	63·2	64·9	65·1	65·7	61·1
Selected CIPW normative minerals												
ab	10·40	10·00	8·26	16·45	24·17	17·59	17·16	18·88	19·91	17·02	21·57	22·22
ne	18·89	7·43	9·24	6·38		3·67	2·29	1·19	4·13	2·83	4·73	3·60
hy					3·63							
ol	18·83	22·35	22·89	18·23	24·40	26·09	21·68	20·08	23·19	19·90	22·98	20·23
Trace elements (ppm)												
Sc	17·4	32·8	n.d.	26·3	26·8	31	33	32·6	29·7	33·5	n.d.	29·9
V	130	n.d.	n.d.	n.d.	163	165	n.d.	201	170	176	n.d.	219
Cr	369	713	n.d.	382	454	449	465	516	360	632	n.d.	365
Rb	72	24	38	32	28	36	20	17	34	19	34	33
Sr	1494	667	640	867	684	691	552	705	715	648	715	603
Y	49	25	23	30	26	31	24	21	28	22	28	24
Zr	500	204	194	236	262	284	158	166	269	165	268	189
Nb	183·2	67·5	70·6	85·3	67·9	66·7	40·3	42·5	67	44·6	67·0	53·9
Mo	9·65	2·43	2·70	3·39	2·28	3·63	2·22	1·65	2·97	2·11	n.d.	2·69
Ba	830	329	431	399	388	361	251	261	345	257	345	358
La	125·1	39·8	40·5	51·8	40·2	41·9	29·3	29·0	37·9	30·2	37·9	35·3
Ce	n.d.	81	86	109	84	88	65	62	69	63	69	69
Pr	28	10	10·2	13·0	10	11	8	8·1	10	8·3	9·6	8·2
Nd	104·3	40·3	39·0	51·2	40·5	41·3	33	33·4	38·8	33·5	39·1	31·9
Sm	18·9	7·7	7·3	9·9	8·1	8·5	6·9	7·1	8·2	7·0	8·2	6·1
Eu	5·7	2·6	2·5	3·2	2·7	2·7	2·4	2·5	2·8	2·5	2·8	2·0
Gd	17·7	8·3	7·7	10·0	8·1	8·7	7·3	7·4	8·4	7·2	8·5	6·5
Tb	2·24	1·06	1·01	1·25	1·05	1·19	1·01	0·9	1·1	0·96	1·1	0·93
Dy	11·8	5·5	5·1	6·5	5·8	6·9	5·5	5·2	6·5	5·0	6·5	5·2
Ho	1·93	1·01	0·89	1·18	0·97	1·21	0·99	0·83	1·07	0·86	1·07	0·92
Er	4·96	2·58	2·25	3·12	2·6	3·28	2·58	2·14	2·69	2·22	2·69	2·53
Tm	0·61	0·33	0·29	0·39	0·32	0·42	0·35	0·26	0·37	0·27	n.d.	0·34
Yb	3·76	2·1	1·87	2·40	2·09	2·69	2·05	1·65	2·18	1·56	2·15	2·29
Lu	0·57	0·29	0·26	0·33	0·27	0·37	0·30	0·23	0·30	0·21	0·30	0·32
Hf	12·8	4·99	4·62	5·60	5·33	6·29	4·69	4·08	6·13	3·97	6·13	4·2
Ta	10·25	3·91	4·17	4·78	3·52	3·72	2·57	2·62	3·63	2·61	3·63	3·1
Pb	5	2·1	2·2	2·43	1·8	2·6	1·7	1·7	1·3	1·5	n.d.	3·3
Th	16·65	5·22	5·89	6·05	4·66	5·92	3·43	3·74	4·97	3·22	4·97	4·65
U	4·93	1·46	1·63	1·82	1·33	1·58	1·02	0·88	1·47	0·95	1·47	1·16

MP8, MP32 and MP34 from Armienti *et al*. (2003); SAX20 and MP24 from Orlando *et al*. (1997); MB65b, MB54, MB27, MB78, MB26, MB32 and MB33 from Armienti *et al*. (1991). LOI, loss on ignition; Mg-number = 100 $Mg/(Mg + Fe^{2+})$ with Fe_2O_3/FeO according to Middlemost (1989). Trace elements determined by ICP-MS; n.d., not determined.

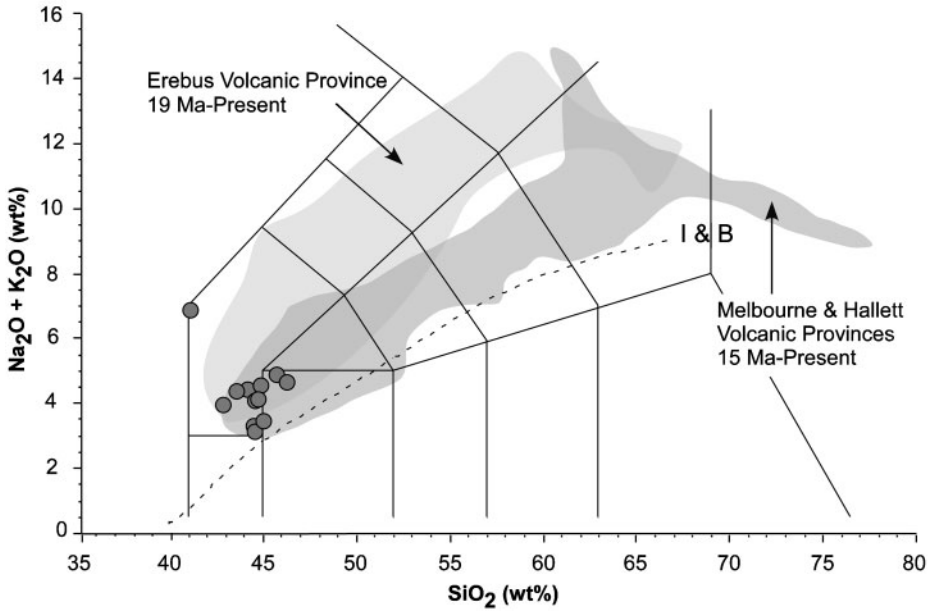

Fig. 2. TAS (total alkalis–silica) diagram (Le Bas *et al.*, 1986). Alkaline–sub-alkaline separation line is from Irvine & Baragar (1971). Grey circles represent analysed samples. For comparison the background fields represent rocks belonging to the volcanic provinces of Mt. Erebus (LeMasurier & Thomson, 1990; Kyle *et al.*, 1992), and Mt. Melbourne and Hallett (LeMasurier & Thomson, 1990; Armienti *et al.*, 1991).

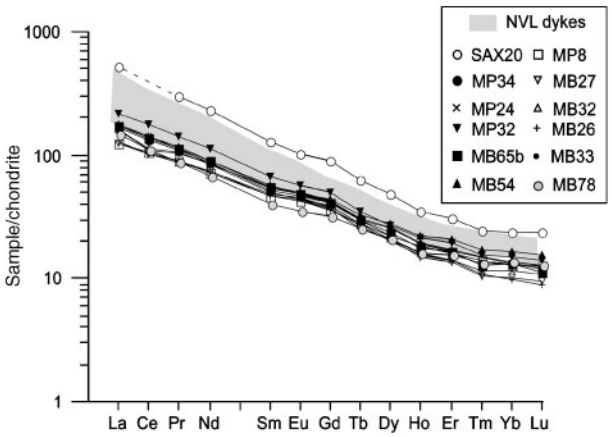

Fig. 3. Chondrite-normalized REE diagram. Normalizing values from McDonough & Sun (1995). For comparison the shaded field represents Cenozoic dykes from northern Victoria Land (Rocchi *et al.*, 2002).

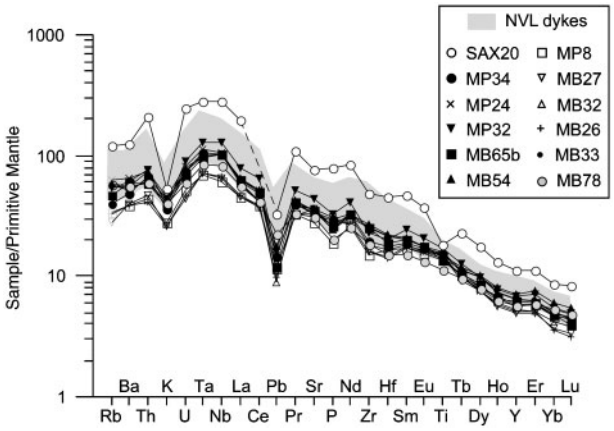

Fig. 4. Primitive Mantle-normalized multi-element diagram. Normalizing values from McDonough & Sun (1995). For comparison the shaded field represents Cenozoic dykes from northern Victoria Land (Rocchi *et al.*, 2002).

temperatures of 1260–1280°C (Orlando *et al.*, 1997). The very low crystal content and the Mg-rich composition of the olivines suggest that their host magmas are close to their liquidus. Consequently, these T values are probably similar to the potential temperature of the mantle source of these melts (Green & Falloon, 2005).

He isotope ratios

Early formed Fe–Mg phenocryst minerals (olivine and pyroxene), grown before extensive degassing and crustal contamination, may preserve the noble gas isotopic signature of the mantle source. In particular, olivine contains negligible U and Th compared with clinopyroxene and is therefore less susceptible to radiogenic ^{4}He ingrowth. The olivine in the selected samples trapped magmatic volatiles in primary melt inclusions (Orlando *et al.*, 1997). We report the noble gas data in Table 3.

Values for ^{3}He/^{4}He from the NVL range between $5{\cdot}73 \pm 0{\cdot}15$ and $7{\cdot}22 \pm 0{\cdot}26$ R_a and ^{40}Ar/^{36}Ar vary between the atmospheric value of about 300 (air 295·5) and a

Table 2: Sr, Nd and Pb isotope ratios measured for whole-rock samples

Sample	$^{87}Sr/^{86}Sr$	$^{143}Nd/^{144}Nd$	$\varepsilon_{Nd\ (t=0)}$	$^{208}Pb/^{204}Pb$	2σ	$^{207}Pb/^{204}Pb$	2σ	$^{206}Pb/^{204}Pb$	2σ
SAX20	0·702840	0·512979	6·7	38·9781	0·0066	15·5399	0·0024	19·5683	0·0030
MP24	0·703160	0·512876	4·8	39·2801	0·0072	15·5665	0·0027	19·6465	0·0036
MP32	0·702854	n.d.	—	39·2857	0·0116	15·5955	0·0044	19·7314	0·0041
MB65b	0·702989	0·512955	6·2	39·0863	0·0049	15·5705	0·0019	19·5581	0·0024
MB54	0·703093	0·512930	5·7	39·2095	0·0146	15·5910	0·0047	19·4497	0·0049
MP8	0·703357	0·512902	5·3	39·2011	0·0081	15·5169	0·0031	19·6407	0·0032
MB27	0·703351	0·512937	5·8	39·1289	0·0364	15·5547	0·0143	19·5564	0·0157
MB32	0·702898	0·512955	6·2	38·7188	0·0085	15·4074	0·0033	19·5349	0·0041
MB26	0·703291	0·512953	6·2	38·9189	0·0058	15·5154	0·0022	19·4601	0·0026
MB33	0·702830	0·512958	6·3	39·1392	0·0079	15·5487	0·0031	19·7446	0·0038
MB78	0·703376	0·512883	5·0	39·1663	0·0090	15·5921	0·0030	19·3481	0·0028

n.d., not determined. $^{87}Sr/^{86}Sr$ corrected for mass fractionation using $^{86}Sr/^{88}Sr = 0{\cdot}1194$ and reported relative to $0{\cdot}710200 \pm 0{\cdot}000008$ for NIST SRM 98. $^{143}Nd/^{144}Nd$ corrected for mass fractionation using $^{146}Nd/^{144}Nd = 0{\cdot}7219$ and reported relative to La Jolla standard $^{143}Nd/^{144}Nd = 0{\cdot}511857 \pm 0{\cdot}000007$. εNd calculated relative to present-day $^{143}Nd/^{144}Nd = 0{\cdot}512638$. External precision for Sr and Nd was better than 0·000010 (2σ) for each measurement. Pb measurements reported relative to NBS 981 $^{208}Pb/^{204}Pb = 37{\cdot}0613 \pm 0{\cdot}0312$, $^{207}Pb/^{204}Pb = 15{\cdot}6061 \pm 0{\cdot}0096$, $^{206}Pb/^{204}Pb = 17{\cdot}0199 \pm 0{\cdot}0070$.

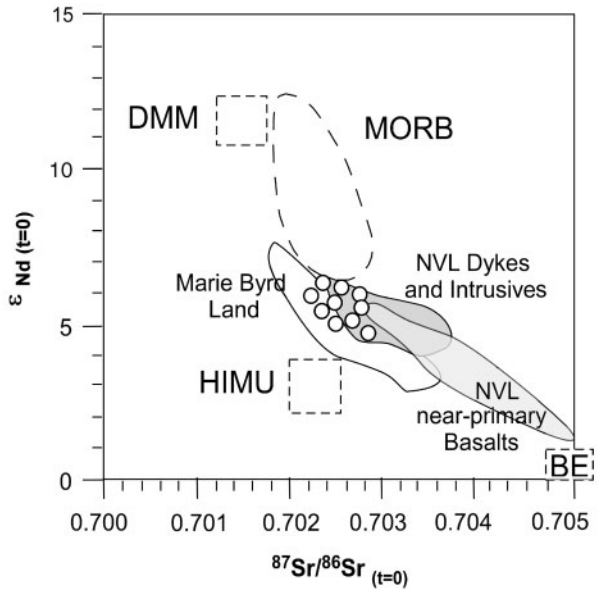

Fig. 5. Isotope correlation diagram including mid-ocean ridge basalts (MORB) from Hofmann (1997) and three end-members after Zindler & Hart (1986): DMM, Depleted MORB Mantle; HIMU, high $^{238}U/^{204}Pb$ ratio; BE, Bulk Earth. {○}, analysed samples. For comparison the fields represent isotopic data from Marie Byrd Land for OIB (Hole & LeMasurier, 1994; Hart *et al.*, 1997; Panter *et al.*, 2000) and from northern Victoria Land (NVL) for near-primary basalts (Rocholl *et al.*, 1995), dykes and intrusive rocks (Rocchi *et al.*, 2002).

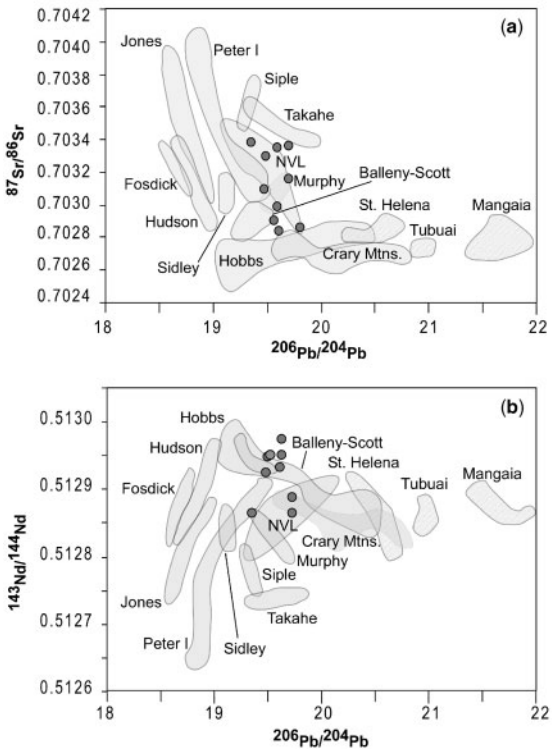

Fig. 6. (a) $^{87}Sr/^{86}Sr$ and (b) $^{144}Nd/^{143}Nd$ vs $^{206}Pb/^{204}Pb$ isotope correlation diagrams for NVL primitive basalts (grey circles) in comparison with other West Antarctic basalts, including those from the Ross Sea Region and Marie Byrd Land (Hart, 1988; Hart *et al.*, 1995, 1997; Rocholl *et al.*, 1995; Panter *et al.*, 2000). Also shown are the extreme HIMU compositions from oceanic islands (Tubuai, St. Helena and Mangaia). Redrawn from Panter *et al.* (2000).

Table 3: Range of forsterite contents of analysed olivine by EMPA-WDS

Sample	Fo (mol %)	$\delta^{18}O$	$\pm1\sigma$	Weight* (g)	^4He (STP cm^3/g)	$^3He/^4He$ R_c	$^3He/^4He$ R/R_a	$\pm1\sigma$	$^4He/^{40}Ar$	$\pm1\sigma$	$^3He/^{40}Ar$ R_a	$\pm1\sigma$
SAX20	89–92	5·36	0·04	0·15	1·16E–08	6·45	6·45	0·29	0·24	7·31E–03	1·52	0·10
MP34	64–92	5·13	0·03	n.d.	—	—	—	—	—	—	—	—
MP24	86–88	5·33	0·16	0·60	1·14E–08	5·76	5·76	0·17	0·18	5·37E–03	1·01	0·04
MB65b	84	5·35	0·05	5·35	4·09E–09	6·53	6·53	0·22	0·58	1·78E–02	3·77	0·19
MB54	90	5·51	0·02	5·51	6·23E–08	6·84	6·83	0·16	0·49	1·51E–02	3·38	0·12
MP8	83–89	5·48	0·10	n.d.	—	—	—	—	—	—	—	—
MB27	83–84	5·02	0·07	0·41	9·82E–09	7·12	7·12	0·22	1·44	4·40E–02	10·26	0·47
MB32	67–88	4·92	0·14	0·31	4·00E–08	6·52	6·52	0·16	0·24	7·25E–03	1·56	0·06
MB26	82–85	5·34	0·07	0·62	5·75E–09	7·22	7·22	0·27	0·35	1·10E–02	2·52	0·14
MB33	67–91	5·53	0·01	n.d.	—	—	—	—	—	—	—	—
MB78	66–85	5·26	0·04	0·16	5·66E–08	5·73	5·73	0·15	0·37	1·13E–02	2·09	0·08

*Weight is for noble gas analysis.
Oxygen isotope ratios ($\delta^{18}O$ VSMOW ‰) are mean values of two analyses for each sample. n.d., not determined. $^3He/^4He$ R_c is the helium isotope ratio corrected for atmospheric helium. $^3He/^4He$ R/R_a is the isotope ratio measured, where the R_a value is the atmospheric $^3He/^4He = 1{\cdot}39 \times 10^{-6}$.

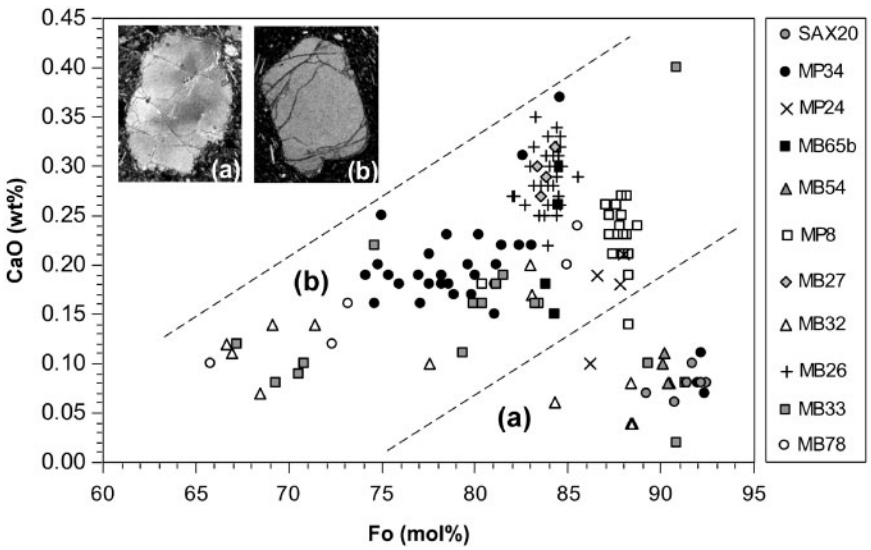

Fig. 7. CaO (wt %) vs Fo (mol %) of analysed olivine: (a) typical habit and composition of olivine xenocrysts; (b) typical euhedral habit and composition of magmatic olivine.

slightly more radiogenic value of 750. To remove any influence of atmospheric helium contamination within these analyses, air contamination corrections were applied (Harrison *et al.*, 2004), indicating negligible contamination effects (shifts in $^3He/^4He$ were typically $\leq 0{\cdot}01$ R_a). It is necessary also to consider whether post-eruption radiogenic ^4He ingrowth or cosmogenic ^3He has affected the measured $^3He/^4He$. It should be noted that both these processes produce nuclides that are sited in the crystal matrix. All the analyses were performed using a pressure fracturing mechanism to release volatiles from the samples (Burnard *et al.*, 2003). Pressure fracturing crushers are designed to release volatiles from fluid inclusions and not matrix-sited volatiles. Only a single step was performed on each sample and the crushing efficiency was of the order of 10–15%. This degree of crushing is highly unlikely to release any significant amounts of matrix-sited gases (Scarsi, 2000). Moreover, crushing efficiency was approximately the same for all samples, thus allowing a comparison between samples. The helium measured can therefore

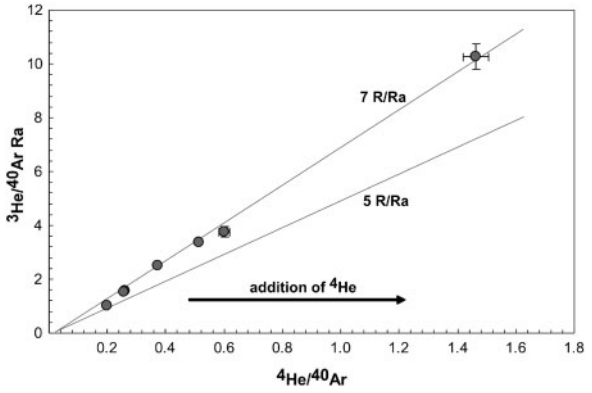

Fig. 8. ^{3}He vs ^{4}He normalized to ^{40}Ar. Error bars are shown for each measurement separately.

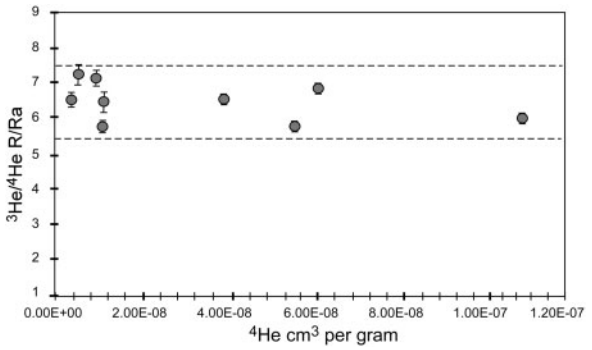

Fig. 9. ^{3}He/^{4}He ratio vs ^{4}He. Error bars are shown for each measurement separately.

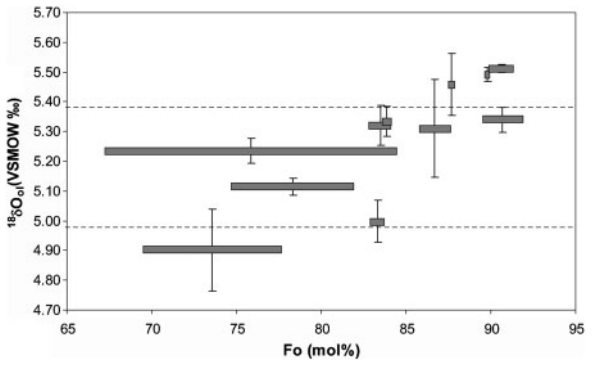

Fig. 10. Fo (mol %) contents of olivine vs oxygen isotope composition ($\delta^{18}O_{ol}$ VSMOW ‰) relative to each sample. Horizontal bars encompass the compositional range of olivine. Vertical error bars represent the 2σ of $\delta^{18}O$ values measured for each sample and are centred on average compositions. Dashed lines delimit the $\delta^{18}O$ range of olivine from xenolithic upper mantle peridotites and MORB sources (5·2 ± 0·2; Eiler *et al.*, 1997).

be considered representative of the fluid inclusions hosted by the phenocrysts.

In Fig. 8 ^{3}He is plotted against ^{4}He, normalized to ^{40}Ar. Two lines are plotted that represent $7R_a$ and $5R_a$ at variable helium/argon ratios and therefore helium concentrations. The addition of excess radiogenic ^{4}He would cause the data to deviate to the right as shown by the arrow on the diagram. All the data plot between the two modelled compositions. Figure 9 is a helium isotope vs ^{4}He concentration diagram. This re-emphasizes that the helium isotope compositions are not controlled by the concentration of radiogenic ^{4}He and can thus be considered representative of the magmatic source. Also, plotting helium isotope ratios against the forsterite content of the analysed olivine (or Mg-number; not shown) shows no correlation. This reveals that magma differentiation had no effect on the He mantle signature.

O isotope ratios

Oxygen isotopic compositions of olivine are listed in Table 3. Measured oxygen isotope ratios range from 4·92 to 5·53‰. Separated olivines, rather than whole-rock powders, have been analysed to avoid any possible effects of post-eruptive alteration (Muehlenbachs, 1986; Harmon & Hoefs, 1995). In addition, olivine crystallizes early in the magmatic evolution of basaltic lavas and is present as a major constituent in the mantle, therefore the effects of fractionation during crystallization or low degrees of partial melting are minimal (Taylor & Sheppard, 1986; Harmon & Hoefs, 1995). No correlation between olivine $\delta^{18}O$ and ^{3}He/^{4}He ratios exist. The absence of correlations between $\delta^{18}O_{ol}$ and whole-rock SiO_2, MgO or Mg-number, and Fe contents, which might be expected, could reflect the presence of cumulus olivine in the basalts. However, the positive correlation between $\delta^{18}O_{ol}$ and Fo content ($R^2 = 0{\cdot}63$) indicates that oxygen isotope composition of olivine was not controlled by crystallization from progressively differentiating magmas (Fig. 10). An exception to this trend is represented by one of the HP–HT olivines, which shows a low $\delta^{18}O$ value (sample MB27 with $\delta^{18}O_{ol} = 5{\cdot}0$‰).

DISCUSSION

Origin of oxygen isotope variability

Most mantle-derived magmas span a narrow range in $\delta^{18}O$ values [i.e. $\delta^{18}O_{ol}$ between ~5·0 and 5·4‰, or $\delta^{18}O_{melt}$ between ~5·4 and 5·6‰ (Eiler, 2001)], which implies that recycled crustal materials are absent in the mantle source or are less than a few per cent. Analysed samples that are outside this range require specific explanations for the origin of the isotopically anomalous material in the mantle source region. The measured oxygen isotope ratios in olivine crystals from this study range from 4·92 to 5·53‰; thus they only slightly deviate from the unmodified mantle composition. However, the $\delta^{18}O_{ol}$ decreasing trend with decreasing Fo content suggests a possible contribution of a low $\delta^{18}O$ contaminant at mantle depths during olivine crystallization. The only major Earth reservoir with a $\delta^{18}O$ value significantly lower than

average mantle is the hydrosphere; crustal rocks can record this value as a result of high-temperature water–rock interaction. The greatest volume of low $\delta^{18}O$ rocks produced by this process is in the oceanic lithosphere, which undergoes extensive hydrothermal alteration at mid-ocean ridges (Shanks, 2001).

Two main processes occurring at mantle conditions may account for the observed low $\delta^{18}O$ values: recycling of subducted hydrothermally altered lower oceanic lithosphere (Eiler *et al.*, 1997; Eiler, 2001) and/or assimilation of low $\delta^{18}O$ wall-rocks during the course of magma crystallization. A key aspect of all low $\delta^{18}O$ components is that they must be sampled in large mass fractions to produce measurable decreases in the $\delta^{18}O$ of basaltic lavas. Mass-balance calculations indicate that lowering the $\delta^{18}O$ average value of olivine crystallized from a primary mantle melt from 5·5 to 4·9‰ would require at least 10% of a contaminant with $\delta^{18}O \sim 0$‰ (i.e. the lowest portions of oceanic lithosphere sampled as a subducted component or shallow-level contaminant). The fact that one of the HP–HT olivines shows a depleted $\delta^{18}O$ value (sample MB27 with $\delta^{18}O = 5{\cdot}0$‰), highlights the possibility that the mafic melts originated from a heterogeneous source that had already inherited a low $\delta^{18}O$ signature. Accordingly, higher Fo olivines crystallized from the more basic magmas, which preserved their original heterogeneous $\delta^{18}O$ values, whereas lower Fo olivines crystallized from slightly more evolved magmas, which received a greater input of the low $\delta^{18}O$ component during their rise through the mantle lithosphere (Eiler *et al.*, 1997; Garcia *et al.*, 1998).

The possible interpretations of the contamination process are: (1) assimilation of the ultramafic portions of subducted oceanic lithosphere with low $\delta^{18}O$ values resulting from seawater–rock interaction at a mid-ocean ridge prior to subduction (Muehlenbachs, 1986; Hart *et al.*, 1999; Panter *et al.*, 2003); (2) assimilation of hydrothermally altered intrusive igneous rocks emplaced within the upper crust during the Middle Eocene (Dallai *et al.*, 2001); (3) assimilation of material from hydrothermally altered volcanic edifices (Widom & Farquhar, 2003; Wang & Eiler, 2008). Because the studied basalts show no evidence of Sr–Nd–Pb isotope variation or major or trace element systematics typical of crustal contamination, the contaminant needs to be similar in composition to the primary basalts. The lack of oceanic lithosphere (vs thinned continental lithosphere) in the Ross Sea region and the nature of the mostly acidic (not mafic) hydrothermally altered intrusive rocks suggest that hydrothermally altered volcanic edifice rocks are the likely effective agents of contamination.

No plume evidence from Helium isotope data

High $^3He/^4He$ ratios (up to 50 R_a, Stuart *et al.*, 2003) have generally been used to argue that the deeper mantle is relatively undegassed and preserves its primordial volatile composition compared with the MORB source region, which has a lower time-integrated $^3He/(U + Th)$ ($\sim$8 R_a, Graham, 2002; Harrison & Ballentine, 2005); however, some attention should be paid to shallower mantle processes (Meibom *et al.*, 2003).

The $^3He/^4He$ ratios of the NVL basalts are $\sim$6–7 R_a and, as previously argued, can be considered as representative of the helium isotope signature of their mantle source. These data are similar to lithospheric mantle values (Gautheron & Moreira, 2002) and overlap the lower limit for some MORB data (Harrison *et al.*, 2003). The He isotope ratios do not support the involvement of deep undegassed material (i.e. a mantle plume) in the genesis of NVL alkaline basaltic melts. In this context the helium isotope data provide an important constraint on the Ross Sea Cenozoic magmatism, for which a plume model must probably be excluded.

The mantle source of the rift-related magmas

Cenozoic basaltic rocks from northern NVL are weakly porphyritic with high Mg-number and Cr contents that indicate compositions close to primary magmas, and thus are suitable samples with which to investigate the nature of their mantle source. Moreover, olivine–melt equilibrium indicates T of about 1200–1300°C, in agreement with the homogenization temperatures found by Orlando *et al.* (1997) for melt inclusions hosted in olivine. To reconstruct the liquidus curve and to establish the phase relations of a near-primary magma (basanite MP24), Orlando *et al.* (2000) carried out several high-T, high-P experiments. Their results suggested that the basanite could have been generated by partial melting either of a spinel lherzolite (at $P = 1{\cdot}5$–$2{\cdot}0$ GPa and $T = 1390$–1490°C) or of a garnet pyroxenite (at $P > 3{\cdot}0$ GPa and $T > 1550$°C).

Further insights into the relationships between the mantle source(s) and the partial melts are provided by the CaTs–Ol–SiO_2 projection (Fig. 11), in which the less evolved basalts are plotted along with some relevant experimental results. The presence of compositions lying on the En–CaTs join provides strong evidence for an origin from a pyroxenitic source when we consider the evident role of this join as a thermal barrier, which is active at $P > 2$ GPa (Hirschmann *et al.*, 2003). On the other hand, some *ne*-normative compositions, plotting just to the left of the boundary, are compatible with the experimental data of Hirschmann *et al.* (1998) and seem to be related to partial melting of a peridotitic source. However, the most undersaturated compositions plot on the pyroxenite melting trend suggested by the high-pressure experiments of Keshav *et al.* (2004), providing an unambiguous marker of the occurrence in the mantle source of pyroxenite domains. These mantle pyroxenites may represent either deep fractionates of parental melts generated on the thermal

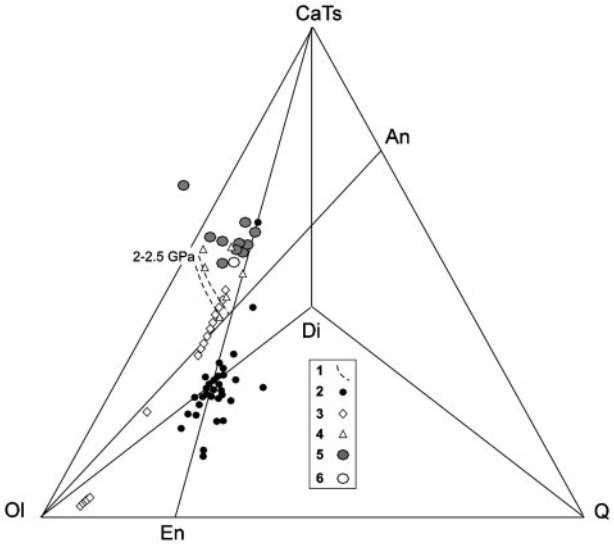

Fig. 11. Projection of major element data on the CaTs–Ol–Q face of the CaTs–Ol–Di–Q tetrahedron (Armienti & Gasperini, 2007). Overview of experimental data on partial melts of pyroxenites from various sources: (1) Keshav *et al.*, 2004; (2) Falloon *et al.*, 2001; (3) Hirschmann *et al.*, 1998; (4) Hirschmann *et al.*, 2003; (5) NVL samples (this work); (6) *hy*-normative samples from NVL (this work).

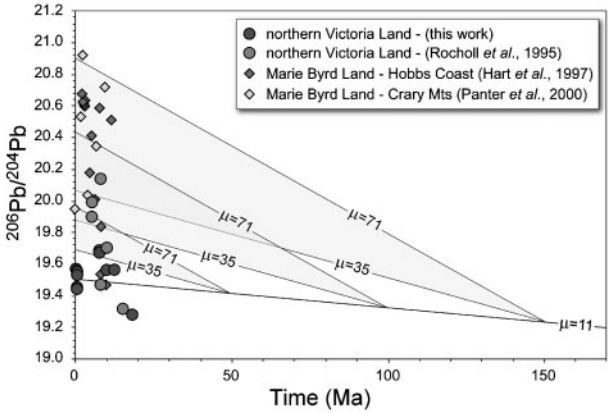

Fig. 12. Conceptual model for the Pb isotopic evolution of the lithospheric mantle beneath the WARS. The evolution of a FOZO-like mantle source is represented with $\mu = 11$. Metasomatic episodes leading to an increase of the U/Pb ratio of the starting FOZO-like mantle are hypothesized at 150, 100 and 50 Ma, with subsequent evolution of the metasomatized domain with μ in the range 35 to 71.

divide or the source itself of the nepheline-normative melts, or both. Possible minor fractionations of ± olivine ± pyroxene would not affect these relationships. In this context, the variable degree of silica saturation of the NVL near-primary melts can be accounted for by a two-step process. First, melts that are more enriched in Mg and less saturated in SiO_2 are derived from the partial melting of a peridotitic source, producing pyroxenite domains. Second, these pyroxenite domains can themselves become the source of subsequent partial melts which are less enriched in Mg and less undersaturated.

The trace element distribution patterns (Fig. 4) are dominated by high ratios of Nb and Ta to LILE and Y–heavy REE (HREE) and high La/K. Multi-element patterns normalized to the Primordial Mantle composition display the typical shape of OIB (McDonough & Sun, 1995). Ba/Rb and La/Nb ratios display typical OIB values, ranging respectively between 10 and 16 (in contrast to Ba/Rb = 5 and 28 in average upper and lower crust, respectively) and between 0·6 and 0·7 (in contrast to La/Nb = 2·2 of continental crust), and Ba/Nb ratios are very low and constant (5–7, in contrast to crustal reservoirs for which Ba/Nb ranges between 20 and 150), indicating the lack of significant crustal contamination.

The overall enrichment of incompatible elements, as well as the Sr–Nd–Pb isotopic ratios, highlights the contribution of a HIMU-like component to the genesis of the studied samples. This feature seems to be common throughout the WARS (Hart & Kyle, 1994; Hart *et al.*, 1997; Panter *et al.*, 2000, 2003) with $^{206}Pb/^{204}Pb$ values varying between 19·3 and 20·1 in the western Ross Sea region, whereas in Marie Byrd Land $^{206}Pb/^{204}Pb$ values vary between 19·5 and 20·9 (Hart *et al.*, 1997; Panter *et al.*, 2000). Such high $^{206}Pb/^{204}Pb$ values are commonly thought to be derived from deep mantle plumes that include slab materials recycled into the deep mantle over a time period of the order of 10^9 a. However, it has been suggested that similarly high $^{206}Pb/^{204}Pb$ ratios in ocean island settings could also result from the enrichment in U relative to Pb of the magma source at rather shallow depths over a time interval of the order of 10^8 a, similar to the age of the adjacent oceanic lithosphere (Halliday *et al.*, 1995). Furthermore, it is increasingly recognized that HIMU sources may also exist within the sub-continental lithosphere, generated by the infiltration of metasomatic fluids and melts (Stein *et al.*, 1997; Pilet *et al.*, 2005, 2008).

Evidence for metasomatic enrichment processes in the source of the NVL Cenozoic basalts is found in peridotite xenoliths containing amphibole veins and/or pyroxenitic portions with dominant amphibole (Coltorti *et al.*, 2004; Perinelli *et al.*, 2006). These amphiboles could have originated by metasomatic reaction of pre-existing clinopyroxene with a metasomatizing Na-alkaline, highly undersaturated, hydrous silicate melt (Coltorti *et al.*, 2004). This type of veined mantle source readily explains the occurrence of K and Ti (for nephelinitic samples) negative anomalies in the trace element distribution patterns in terms of residual amphibole and/or phlogopite in the mantle source.

Knowledge of the age(s) of this(these) metasomatic event(s) is necessary to improve the geodynamic timeframe of the generation of the magma sources. A rough,

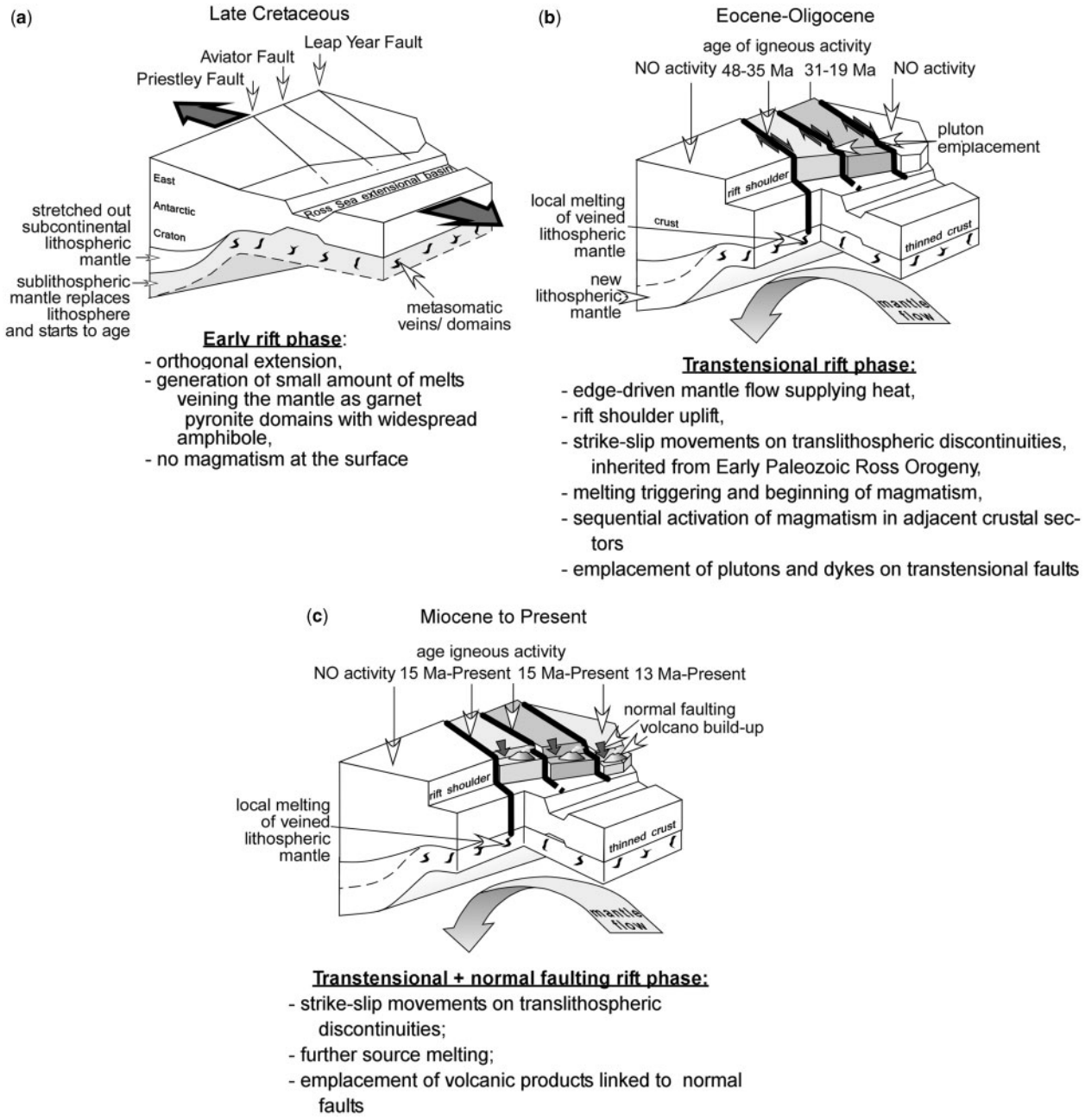

Fig. 13. General model for the Mesozoic–Cenozoic tectonomagmatic history of the western Ross Embayment.

yet very useful estimate of such an age can be obtained based on the assumption of a two-stage (Finn *et al.*, 2005) or a multi-stage (Lucassen *et al.*, 2008) mantle evolution, as suggested by petrological constraints. In this context, our modelling assumes that a Bulk Earth–FOZO mantle composition is affected by one or more (auto)metasomatic events, increasing its U/Pb ratio. In detail, the starting mantle composition lies on the evolution line of the ubiquitous FOZO-like mantle, which with a U/Pb value of 0·16 would lead to a present-day $^{206}Pb/^{204}Pb$ of 19·5. Lead isotope compositions attained at 150, 100 and 50 Ma benchmarks are assumed as further starting points to calculate the Pb isotopic evolution of metasomatically enriched domains in which the U/Pb ratio was increased to values between 0·5 and unity (a value 10% lower than the maximum observed in our samples to take into account the slightly lower incompatibility of U with respect to Pb during melting).

The modelling (Fig. 12) shows that even the highest $^{206}Pb/^{204}Pb$ values observed for Marie Byrd Land lavas (20·9: Hart *et al.*, 1997; Panter *et al.*, 2000) can be obtained by invoking a metasomatic event at about 150 Ma, significantly younger than that suggested by Finn *et al.* (2005) and Panter *et al.* (2006). In particular, the $^{206}Pb/^{204}Pb$ values observed for the NVL lavas (varying from FOZO-like values to 20·1) can be obtained via two different mechanisms. The first scenario yields HIMU-like Pb isotopic values by means of a moderately recent metasomatic event (100 Ma), which increased the source U/Pb ratios to values of about 0·8. The intermediate values are compatible with melting of a source affected by a more recent metasomatic event (50 Ma), leading to high U/Pb values of unity. The melts with FOZO-like $^{206}Pb/^{204}Pb$ ratios would be derived from a source that was not affected by metasomatism.

A simpler, hence preferred, alternative scenario, takes into account the possibility that the melts were derived from variable contributions of metasomatic veins or domains and the surrounding mantle. Specifically, the enriched mantle domains created during the Late Cretaceous and isotopically matured since then underwent a process of 'sampling upon melting and averaging' (Meibom & Anderson, 2004). In this scenario, the isotopic variations of the magmas are linked to slightly different scales of sampling the mantle heterogeneity during melt production and/or averaging during melt collection.

The modelling results, coupled with the high U/Pb of the studied lavas, indicate that a likely age for the metasomatism affecting the source of NVL magma could be set in the Late Cretaceous, when a major event of amagmatic orthogonal extension affected the WARS. Lithospheric thinning allowed the rise of the weaker sublithospheric mantle and led to the production of very small degree partial melts, not sufficient to feed surface magmatism (amagmatic rift phase). However, these melts were essential in distributing fertile, enriched, low-melting point veins or domains through a wide zone of the Antarctic plate mantle. This mantle and its metasomatic domains started to age, becoming progressively the new lithospheric mantle underlying the WARS.

CONCLUSIONS

The data presented here support a model for the origin of the Cenozoic basaltic magmas of the NVL from a sublithospheric mantle source metasomatized during an extensional event that affected the WARS in the Late Cretaceous (Fig. 13a). After metasomatism, the sublithospheric mantle started to age and was rheologically incorporated into the lithosphere. The link between the Cenozoic geodynamic evolution of the WARS region and the development of the source-melt system is illustrated in the following scenario.

During Eocene–Oligocene times, mantle flow under the extended, thinned part of the WARS, directed towards the thick Antarctic Craton (Figure 13b), provided the heat to warm the mantle at the edge of the thick Antarctic lithosphere (Faccenna *et al.*, 2008). In the Middle Eocene, the increase in differential velocity across the Southern Ocean fracture zones reactivated Palaeozoic tectonic discontinuities in northern Victoria Land as intraplate dextral strike-slip fault systems (Rocchi *et al.*, 2003, 2005; Storti *et al.*, 2007). The activity of these lithospheric deformation belts induced local mantle decompression melting. Emplacement of the rising magmas as plutons and dyke swarms was related to the main NW–SE discontinuities (Rocchi *et al.*, 2002).

From Late Miocene to Present, the continuing craton-directed mantle flow led to collapse of the rift shoulder and normal faulting (Faccenna *et al.*, 2008), which favoured the rise of magmas to the surface and the construction of large volcanic edifices along north–south normal-transtensional faults arrays departing from the master NW–SE systems (Fig. 13c).

ACKNOWLEDGEMENTS

This work is dedicated to the memory of Filippo Olmi (EMPA-WDS) for his human and scientific values. The authors wish to thank M. Bertoli (wet chemistry), M. D'Orazio (ICP-MS), G. De Grandis (mineral separations), A. Dini (Pb isotopes), M. Tamponi (XRF) and S. Tonarini (Sr and Nd isotopes) for their expert assistance during laboratory work. We are grateful to Kurt Panter, Godfrey Fitton, Phil Leat and Keith Putirka for journal reviews, which led to a significant improvement of the original manuscript. This work was financially supported by Programma Nazionale di Ricerche in Antartide (PNRA).

REFERENCES

Armienti, P. & Baroni, C. (1999). Cenozoic climatic change in Antarctica recorded by volcanic activity and landscape evolution. *Geology* **27**(7), 617–620.

Armienti, P. & Gasperini, D. (2007). Do we really need mantle components to define mantle compositions? *Journal of Petrology* **48**, 693–709.

Armienti, P., Civetta, L., Innocenti, F., Manetti, P., Tripodo, A., Villari, L. & Vita, G. (1991). New petrological and geochemical data on Mt. Melbourne volcanic field, northern Victoria Land, Antarctica. (II Italian Antarctic expedition). *Memorie della Società Geologica Italiana* **46**, 397–424.

Armienti, P., Francalanci, L., Landi, P. & Vita, G. (2003). Age and geochemistry of volcanic rocks from Daniell Peninsula and Coulman Island, Hallett Volcanic Province, Antarctica. In: Tessensohn, F. & Ricci, C. A. (eds) *Aspects of a Suture Zone. Geologisches Jahrbuch, Polar Issue 9*, pp. 409–445.

Asprey, L. B. (1976). The preparation of very pure F_2 gas. *Journal of Fluorine Chemistry* **7**, 359–361.

Behrendt, J. C., LeMasurier, W. E., Cooper, A. K., Tessensohn, F., Tréhu, A. & Damaske, D. (1991). Geophysical studies of the West Antarctic Rift System. *Tectonics* **10**(6), 1257–1273.

Bence, E. & Albee, A. (1968). Empirical correction factors for the electron microanalyses of silicates and oxides. *Journal of Geology* **76**, 382–403.

Burnard, P. G., Harrison, D., Turner, G. & Nesbitt, R. (2003). The degassing and contamination of noble gases in mid-Atlantic Ridge basalts. *Geochemistry, Geophysics, Geosystems* doi:10.1029/2002GC000326.

Clayton, R. N. & Mayeda, T. (1983). Oxygen isotopes in eucrites, shergottites, nakhlites, and chassignites. *Earth and Planetary Science Letters* **62**, 1–6.

Coltorti, M., Beccaluva, L., Bonadiman, C., Faccini, B., Ntaflos, T. & Siena, F. (2004). Amphibole genesis via metasomatic reaction with clinopyroxene in mantle xenoliths from Victoria Land, Antarctica. *Lithos* **75**, 115–139.

Dallai, L., Ghezzo, C. & Longinelli, A. (2001). Fossil hydrothermal systems tracking Eocene climate change in Antarctica. *Geology* **29**(10), 931–934.

Della Vedova, B., Pellis, G., Trey, H., Zhang, J., Cooper, A. K. & Makris, J. & the ACRUP Working Group (1997). Crustal structure of the Transantarctic Mountains. In: Ricci, C. A. (ed.) *The Antarctic Region: Geological Evolution and Processes, Terra Antarctica*, Proceedings of the 7th International Symposium on Antarctic Earth Sciences. Siena: Italy, pp. 609–618.

D'Orazio, M. (1995). Trace elements determination in igneous rocks by ICP-MS: results on ten international reference samples. *Periodico di Mineralogia* **64**, 315–328.

Eiler, J. M. (2001). Oxygen isotope variations of basaltic lavas and upper mantle rocks. In: Valley, J. W. & Cole, D. R. (eds) *Stable Isotope Geochemistry. Mineralogical Society of America, Reviews in Mineralogy and Geochemistry* **43**, 319–364.

Eiler, J. M., Farley, K. A., Velley, J. W., Hauri, E., Craig, H., Hart, S. R. & Stolper, E. M. (1997). Oxygen isotope variations in ocean island basalt phenocrysts. *Geochimica et Cosmochimica Acta* **61**, 2281–2293.

Faccenna, C., Rossetti, F., Becker, T.W., Danesi, S. & Morelli, A. (2008). Recent extension driven by mantle upwelling beneath the Admiralty Mountains (East Antarctica). *Tectonics* **27**, TC4015, doi:4010.1029/2007TC002197.

Falloon, T. J., Danyushevsky, L. V. & Green, D. H. (2001). Peridotite melting at 1 GPa; reversal experiments on partial melt compositions produced by peridotite–basalt sandwich experiments. *Journal of Petrology* **42**, 2363–2390.

Finn, C. A., Dietmar Müller, R. & Panter, K. S. (2005). A Cenozoic diffuse magmatic province (DAMP) in the southwest Pacific province without rift or plume origin. *Geochemistry, Geophysics, Geosystems* **4**(8) doi:10.1029/2004GC000723.

Garcia, M. O., Ito, E., Eiler, J. M. & Pietraszka, A. J. (1998). Crustal contamination of Kilauea volcano magmas revealed by oxygen isotope analyses of glass olivine from Puu Oo eruption lavas. *Journal of Petrology* **39**, 803–817.

Gautheron, C. & Moreira, M. (2002). Helium signature of the subcontinental lithospheric mantle. *Earth and Planetary Science Letters* **199**, 39–47.

Govindaraju, K. (1994). 1994 compilation of working values and sample description for 383 geostandards. *Geostandards Newsletter* **18**, 1–58.

Graham, D. W. (2002). Noble gas isotope geochemistry of mid-ocean ridge and ocean island basalts: Characterization of mantle source reservoirs. In: Porcelli, D., Ballentine, C.J. & Wieler, R. (eds) *Noble Gas in Geochemistry and Cosmochemistry, Reviews in Mineralogy and Geochemistry, Mineralogical Society of America*. Washington: DC **47**, pp. 247–318.

Green, D. H. & Falloon, T. J. (2005). Primary magmas at mid-ocean ridges, 'hot-spots' and other intraplate settings: constraints on mantle potential temperature. In: Foulger, G. R., Natland, J. H., Presnall, D. C. & Anderson, D. L. (eds) *Plates, Plumes and Paradigms. Geological Society of America, Special Papers* **388**, 217–218.

Halliday, A. N., Lee, D. C., Tommasini, S., Davies, G. R., Paslick, C. R., Fitton, J. D. & James, D. E. (1995). Incompatible trace elements in OIB and MORB and source enrichment in the sub-oceanic mantle. *Earth and Planetary Science Letters* **133**, 379–395.

Harmon, R. S. & Hoefs, J. (1995). Oxygen isotope heterogeneity of the mantle deduced from global ^{18}O systematics of basalts from different geotectonic settings. *Contributions to Mineralogy and Petrology* **120**, 95–114.

Harrington, H. J. (1958). Nomenclature of rock units in the Ross Sea region, Antarctica. *Nature* **182**, 290.

Harrison, D. & Ballentine, C. J. (2005). Noble gas models of mantle convection and mass reservoir transfer. In: Van der Hilst, R., Bass, J., Matas, J. & Trampert, J. (eds) *Earth's Deep Mantle: Structure, Composition and Evolution. Geophysical Monograph, American Geophysical Union* **160**, 9–26.

Harrison, D., Burnard, P. G. & Turner, G. (1999). Noble gas behaviour and composition in the mantle: constraints from the Iceland Plume. *Earth and Planetary Science Letters* **171**, 199–207.

Harrison, D., Leat, P. T., Burnard, P. G., Turner, G., Fretzdorff, S. & Millar, I. L. (2003). Resolving mantle components in oceanic lavas from segment E2 of the East Scotia back-arc ridge. In: Larter, R. D. & Leat, P. T. (eds) *Intra-Oceanic Subduction Systems: Tectonic and Magmatic Processes. Geological Society, London, Special Publications* **219**, 333–344.

Harrison, D., Barry, T. & Turner, G. (2004). Possible diffusive fractionation of helium isotopes in olivine and clinopyroxene phenocrysts. *European Journal of Mineralogy* **1**, 213–220.

Hart, S. R. (1988). Heterogeneous mantle domains: signature, genesis and mixing chronologies. *Earth and Planetary Science Letters* **9**, 273–296.

Hart, S. R. & Kyle, P. R. (1994). Geochemistry of McMurdo Group volcanic rocks. *Antarctic Journal of the United States* **2**, 14–16.

Hart, S. R., Blusztajn, J. & Craddok, C. (1995). Cenozoic volcanism in Antarctica: Jones Mountains and Peter I Island. *Geochimica et Cosmochima Acta* **59**, 3379–3388.

Hart, S. R., Blusztajn, J., LeMasurier, W. E. & Rex, D. C. (1997). Hobbs Coast Cenozoic volcanism: implications for the West Antarctic rift system. *Chemical Geology* **13**, 223–248.

Hart, S. R., Blusztajn, J., Dick, H. J. B., Meyer, P. S. & Muehlenbachs, K. (1999). The fingerprint of sea-water circulation in a 500-meter section of ocean crust gabbros. *Geochimica et Cosmochima Acta* **6**, 4059–4080.

Hirschmann, M. M., Ghiorso, M. S., Wasylenky, L. E., Asimow, P. D. & Stolper, E. M. (1998). Calculation of peridotite partial melting from thermodynamic models of minerals and melts. I. Review of methods and comparison with experiments. *Journal of Petrology* **39**, 1091–1115.

Hirschmann, M. M., Kogiso, T., Baker, M. B. & Stolper, E. M. (2003). Alkalic magmas generated by partial melting of garnet pyroxenite. *Geology* **6**, 481–484.

Hofmann, A. W. (1997). Mantle geochemistry: The message from oceanic volcanism. *Nature* **38**, 219–229.

Hole, M. J. & LeMasurier, W. (1994). Tectonic controls on the geochemical composition of Cenozoic, mafic alkaline volcanic rocks from West Antarctica. *Contributions to Mineralogy and Petrology* **11**, 187–202.

Irvine, T. N. & Baragar, W. R. A. (1971). A guide to the chemical classification of the common volcanic rocks. *Canadian Journal of Earth Sciences* **8**, 523–548.

Jurewicz, A. J. G. & Watson, E. B. (1988). Cations in olivine, part 1: calcium partitioning and calcium–magnesium distribution between olivine and coexisting melts, with petrologic applications. *Contributions to Mineralogy and Petrology* **9**, 176–185.

Keshav, S., Gudfinnsson, G. H., Sen, G. & Fei, Y. (2004). High-pressure melting experiments on garnet clinopyroxenite and the alkali to tholeiitic transition in oceanic-island basalts. *Earth and Planetary Science Letters* **223**, 365–379.

Kyle, P. R., Moore, J. A. & Thirlwall, M. F. (1992). Petrologic evolution of anorthoclase phonolite lavas at Mount Erebus, Ross Island, Antarctica. *Journal of Petrology* **33**(4), 849–875.

Le Bas, J. M., Le Maitre, R. V., Streckeisen, A. & Zanettin, B. (1986). A chemical classification of volcanic rocks based on the total alkali–silica diagram. *Journal of Petrology* **27**, 745–750.

LeMasurier, W. E. & Landis, C. A. (1996). Mantle plume activity recorded by low relief erosion surfaces in West Antarctica and New Zeland. *Geological Society of America Bulletin* **108**, 1450–1466.

LeMasurier, W. E. & Rex, D. C. (1989). Evolution of linear volcanic ranges in Marie Byrd Land (Antarctica). *Journal of Geophysical Research* **94**(B6), 7223–7236.

LeMasurier, W. E. & Thomson, J. W. (eds) (1990). *Volcanoes of the Antarctic Plate and Southern Oceans, American Geophysical Union*. Washington D. C.: Antarctic Research Series, **48**.

Lucassen, F., Franz, G., Romer, R., Pudlo, D. & Dulski, P. (2008). Nd, Pb, and Sr isotope composition of Late Mesozoic to Quaternary intra-plate magmatism in NE Africa (Sudan, Egypt): high-μ signatures from the mantle lithosphere. *Contributions to Mineralogy and Petrology* **156**(6), 765–784.

Lucchitta, B. K., Bowell, J. A. & Tessensohn, F. (1987). Landsat images for Antarctic research. *Memorie della Società Geologica Italiana* **33**, 35–40.

McDonough, W. F. & Sun, S. S. (1995). The composition of the Earth. *Chemical Geology* **120**, 223–253.

Meibom, A. & Anderson, D. L. (2004). The statistical upper mantle assemblage. *Earth and Planetary Science Letters* **217**, 123–139.

Meibom, A., Anderson, D. L., Sleep, N. H., Frey, R., Chamberlain, C. P., Hren, M. T. & Wooden, J. L. (2003). Are high $^{3}He/^{4}He$ ratios in oceanic basalts an indicator of deep-mantle plume components? *Earth and Planetary Science Letters* **208**, 197–204.

Middlemost, E. A. K. (1989). Iron oxidation ratio, norms and the classification of volcanic rocks. *Chemical Geology* **77**, 9–26.

Muehlenbachs, K. (1986). Alteration of the oceanic crust and the ^{18}O history of seawater. In: Valley, J. W., Taylor, H. P. & O'Neil, J. R. (eds) *Stable Isotopes in High Temperature Geological Processes. Mineralogical Society of America, Reviews in Mineralogy* **16**, 425–444.

Müller, P., Schmidt-Thomé, M., Kreuzer, H., Tessensohn, F. & Vetter, U. (1991). Cenozoic peralkaline magmatism at the western margin of the Ross Sea, Antarctica. *Memorie della Società Geologica Italiana* **46**, 315–336.

Orlando, A., Armienti, P., Conticelli, S., Vaggelli, G. & Manetti, P. (1997). Petrologic investigations on the primitive Cainozoic lavas of Northern Victoria Land, Antarctica. In: Ricci, C. A. (ed.) *The Antarctic Region: Geological Evolution and Processes, Terra Antarctica*. Proceedings of the 7th International Symposium on Antarctic Earth Sciences. Italy: Siena, pp. 523–530.

Orlando, A., Conticelli, S., Borrini, D. & Armienti, P. (2000). Experimental study on a primary basanite from McMurdo Volcanic Group, Antarctica: Inference on its mantle source. *Antarctic Science* **12**(1), 105–116.

Panter, K. S., Hart, S. R., Kyle, P., Blusztanjn, J. & Wilch, T. (2000). Geochemistry of Late Cenozoic basalts from the Crary Mountains: characterization of mantle sources in Marie Byrd Land, Antarctica. *Chemical Geology* **165**, 215–241.

Panter, K. S., Blusztajn, J., Wingrove, D. & Mattey, D. (2003). Sr, Nd, Pb, Os, O isotope, major and trace element data from basalts, south Victoria Land, Antarctica: evidence for open system processes in the evolution of mafic alkaline magmas. *General Assembly of the European Geosciences Union, Geophysical Research Abstracts* **5**, 07583.

Panter, K. S., Blusztajn, J., Hart, S. R., Kyle, P. R., Esser, R. & McIntash, W. C. (2006). The origin of HIMU in the SW Pacific: evidence from intraplate volcanism in southern New Zealand and Subantarctic islands. *Journal of Petrology* **47**, 1673–1704.

Perinelli, C., Armienti, P. & Dallai, L. (2006). Geochemical and O-isotope constraints on the evolution of lithospheric mantle in the Ross Sea rift area (Antarctica). *Contributions to Mineralogy and Petrology* **151**(3), 245, doi:10.1007/S00410-006-0065-8.

Pilet, S., Hernandez, J., Sylvester, P. J. & Poujol, M. (2005). The metasomatic alternative for ocean island basalt chemical heterogeneity. *Earth and Planetary Science Letters* **236**, 148–166.

Pilet, S., Baker, M. B. & Stolper, E. M. (2008). Metasomatized lithosphere and the origin of alkaline lavas. *Science* **320**, 916–919.

Rocchi, S., Armienti, P., D'Orazio, M., Tonarini, S., Wijbrans, J. R. & Di Vincenzo, G. (2002). Cenozoic magmatism in the western Ross Embayment: Role of mantle plume versus plate dynamics in the development of the West Antarctic Rift System. *Journal of Geophysical Research* **107**(B7), doi:10.1029/2001JB000515.

Rocchi, S., Storti, F., Di Vincenzo, G. & Rossetti, F. (2003). Intraplate strike-slip tectonics as an alternative to mantle plume activity for the Cenozoic rift magmatism in the Ross Sea region, Antarctica. In: Storti, F., Holdsworth, R. E. & Salvini, F. (eds) *Intraplate Strike-Slip Deformation Belts. Geological Society, London, Special Publications* **210**, 145–158.

Rocchi, S., Armienti, P. & Di Vincenzo, G. (2005). No plume, no rift magmatism in the West Antarctic Rift. In: Foulger, G. R., Natland, J. H., Presnall, D.C. & Anderson, D. L. (eds) *Plates, Plumes, and Paradigms. Geological Society of America, Special Papers* **388**, 435–447.

Rocholl, A., Stein, M., Molzahan, M., Hart, S. R. & Wörner, G. (1995). Geochemical evolution of rift magmas by progressive tapping of stratified mantle source beneath the Ross Sea rift, Northern Victoria Land, Antarctica. *Earth and Planetary Science Letters* **131**, 207–224.

Roeder, P. L. & Emslie, R. F. (1970). Olivine–liquid equilibrium. *Contributions to Mineralogy and Petrology* **29**, 275–289.

Salvini, F. & Storti, F. (1999). Cenozoic tectonic lineaments of the Terra Nova Bay region, Ross Embayment, Antarctica. *Global and Planetary Change* **23**, 129–144.

Salvini, F., Brancolini, G., Busetti, M., Storti, F., Mazzarini, F. & Coren, F. (1997). Cenozoic geodynamics of the Ross Sea region of Antarctica: crustal extension, intraplate strike-slip faulting and tectonic inheritance. *Journal of Geophysical Research* **102**, 24669–24696.

Scarsi, P. (2000). Fractional extraction of helium by crushing of olivine and clinopyroxene phenocrysts: effects on the $^{3}He/^{4}He$ measured ratio. *Geochimica et Cosmochimica Acta* **64**, 3751–3762.

Shanks, W. C. (2001). Stable isotopes in seafloor hydrothermal systems. In: Valley, J. W. & Cole, D. R. (eds) *Stable Isotope Geochemistry. Mineralogical Society of America, Reviews in Mineralogy* **43**, 469–526.

Sharp, Z. D. (1995). Oxygen isotope geochemistry of the Al_2SiO_5 polymorphs. *American Journal of Science* **295**, 1058–1076.

Stein, M., Navon, O. & Kessel, R. (1997). Chromatographic metasomatism of the Arabian–Nubian lithosphere. *Earth and Planetary Science Letters* **152**, 75–91.

Storey, B. C., Leat, P. T., Weaver, S. D., Pankhurst, R. J., Bradshaw, J. D. & Kelley, S. (1999). Mantle plumes and Antarctica–New Zeland rifting: evidence from mid-Cretaceous mafic dykes. *Journal of Geological Society, London* **156**, 659–671.

Storti, F., Salvini, F., Rossetti, F. & Phipps Morgan, J. (2007). Intraplate termination of transform faulting within the Antarctic continent. *Earth and Planetary Science Letters* **260**(1–2), 115–126.

Stuart, F. M., Lass-Evans, S., Fitton, J. G. & Ellam, R. M. (2003). High $^{3}He/^{4}He$ ratios in picritic basalts from Baffin Island and the role of a mixed reservoir in mantle plumes. *Nature* **424**, 57–59.

Taylor, H. P. & Sheppard, S. M. F. (1986). Processes of isotopic fractionation and isotope systematics. In: Valley, J. W., Taylor, H. P. & O'Neil, J. R. (eds) *Stable Isotopes in High Temperature Geological Processes. Mineralogical Society of America, Reviews in Mineralogy* **16**, 25–444.

Tonarini, S., Rocchi, S., Armienti, P. & Innocenti, F. (1997). Constraints on timing of Ross Sea rifting inferred from Cainozoic intrusions from northern Victoria Land, Antarctica. In: Ricci, C. A. (ed.) *The Antarctic Region: Geological Evolution and Processes*, pp. 511–521.

Vaggelli, G., Olmi, F. & Conticelli, S. (1999). Quantitative electron microprobe analysis of reference silicate mineral and glass samples. *Acta Vulcanologica* **11**(2), 297–303.

Wang, Z. & Eiler, J. M. (2008). Insights into the origin of low-$\delta^{18}O$ basaltic magmas in Hawaii revealed from *in-situ* measurements of oxygen isotope compositions of olivines. *Earth and Planetary Science Letters* **269**, 376–386.

Widom, E. & Farquhar, J. (2003). Oxygen isotope signatures in olivine from São Miguel (Azores) basalts: implications for crustal and mantle processes. *Chemical Geology* **193**, 237–255.

Wilson, T. J. (1999). Cenozoic structural segmentation of the TransantarcticMountains rift flank in southern Victoria Land. *Global and Planetary Change* **23**, 105–127.

Zindler, A. & Hart, S. R. (1986). Helium: problematic primordial signals. *Earth and Planetary Science Letters* **79**, 1–8.

Zipfel, J. & Wörner, G. (1992). Four- and five-phase peridotites from a continental rift system: evidence for upper mantle uplift and cooling at the Ross Sea margin (Antarctica). *Contributions to Mineralogy and Petrology* **111**, 24–36.

APPENDIX: ANALYTICAL METHODS

Whole-rock analyses

Trace elements were determined by inductively coupled plasma-mass spectrometry (ICP-MS) (Fisons PQ2 Plus®) at the Department of Earth Sciences, University of Pisa. Samples were dissolved in screw-top PFA Savillex® vessels on a hot plate at ~120°C with HF–HNO_3 and then analysed following the method reported by D'Orazio (1995). Analyses were performed by external calibration using the BE-N basaltic geochemical reference sample (Govindaraju, 1994). The correction procedure includes: (1) blank subtraction; (2) instrumental drift correction using Rh–Re–Bi internal standardization and repeated (every five samples) analysis of a drift monitor; (3) oxide–hydroxide interference correction. Precision, evaluated by replicate dissolutions and analyses of the in-house standard HE-1 (Mt. Etna hawaiite), was generally between 2 and 5% RDS, except for Gd (6%), Tm (7%), Pb and Sc (8%). Detection limits at 6σ level are in the range of 0·002–0·02 ng/ml in the solution (corresponding to 0·002–0·02 ppm for a 1000-fold sample dilution) for all elements except for Ba, Pb and Sr (0·1–0·2 ng/ml) (D'Orazio, 1995).

Sr and Nd isotopic compositions were determined on whole-rock powders using a Finnigan MAT 262V multicollector mass-spectrometer (dynamic state) at the IGG-CNR, Pisa. $^{87}Sr/^{86}Sr$ was corrected for mass fractionation using $^{86}Sr/^{88}Sr = 0{\cdot}1194$ and $^{143}Nd/^{144}Nd$ was corrected using $^{146}Nd/^{144}Nd = 0{\cdot}7219$. During the collection of isotopic data, 15 replicate analyses of NIST SRM 981 ($SrCO_3$) gave average values of $0{\cdot}710200 \pm 0{\cdot}000008$ (2σ) and 14 analyses of La Jolla standard gave an average $^{143}Nd/^{144}Nd$ of $0{\cdot}511857 \pm 0{\cdot}000007$ (2σ). ε_{Nd} was calculated relative to the present-day $^{143}Nd/^{144}Nd = 0{\cdot}512638$. External precision for Sr and Nd was better than 0·000010 for each measurement. Sr and Nd isotope ratios are given as measured values. No age corrections are necessary because of their young age (<18 Ma) and low Rb/Sr and Sm/Nd ratios.

Pb isotope compositions were determined using a Finnigan MAT 262V multi-collector mass-spectrometer (steady state) at the IGG-CNR, Pisa. During the collection of isotopic data, 15 replicate analyses of the NBS 981 standard gave average values of $^{208}Pb/^{204}Pb$ $37{\cdot}0613 \pm 0{\cdot}0312$ (2σ), $^{207}Pb/^{204}Pb$ $15{\cdot}6061 \pm 0{\cdot}0096$ (2σ) and $^{206}Pb/^{204}Pb$ $17{\cdot}0199 \pm 0{\cdot}0070$ (2σ).

Single mineral analyses

Major and trace elements analyses of olivine separates were obtained at the IGG-CNR, Florence using a JEOL JXA-8600 electron microprobe with four wavelength-dispersive spectrometers at 15 kV accelerating voltage and 10 nA beam current (focused beam of about 1 μm in diameter). The applied matrix correction was according to Bence & Albee (1968). Analytical error agrees with the data reported by Vaggelli *et al.* (1999).

For helium isotope analyses unaltered olivine phenocrysts (0·5–2·0 mm in size), from selected basaltic samples, were ultrasonically cleaned with de-ionized water and finally acetone. After drying, the separates were handpicked under a binocular microscope and then loaded into an online *in vacuo* crusher system. The crusher and neighbouring sections of the stainless steel extraction line were baked at 150°C under vacuum for 12 h to remove any adsorbed atmospheric gases prior to analysis. Helium isotope, neon abundance and argon isotope determinations were performed using an MAP 215 noble gas mass spectrometer at the Department of Earth Sciences, University of Manchester, following the procedures and the measurements protocols of Harrison *et al.* (1999, 2003). Gases extracted by crushing were exposed to a SAES Zr–Al getter operating at 250°C to clean and remove any active

gas (i.e. N_2, O_2 and CO_2) released during sample crushing. After purification, the gases were condensed onto an activated charcoal finger held at liquid nitrogen temperature (−196°C). The non-condensable species, including helium, neon and H_2, were then exposed to another SAES Zr–Al getter, operating at room temperature to reduce any H_2 prior to introduction into the mass spectrometer. A second charcoal finger (held at −196°C), adjacent to the source inlet valve, was used to minimize and stabilize the background levels of any residual argon, CO_2 and H_2O during the helium analysis. ^{20}Ne was measured during the helium run. After helium analysis, the condensable gases were released from the charcoal finger and, prior to expansion into the mass spectrometer for argon analysis, were exposed to a room temperature SAES Zr–Al getter for secondary clean-up. ^{4}He, ^{36}Ar and ^{40}Ar isotopes were measured using a Faraday collector whereas ^{3}He and ^{20}Ne were measured using an electron multiplier in digital pulse counting mode. A resolving power of 650 on the electron multiplier at 5% of the peak height allowed for the complete separation of the $^{3}He^{+}$ beam from any interference by the H_3–HD^{+} doublet. Noble gas abundances were calculated by peak height comparison with a known pressure of calibration gas. Analytical blanks were determined prior to crushing steps.

Oxygen isotopes ratios on olivine separates were measured at the IGG-CNR, Pisa, by conventional laser fluorination (Sharp, 1995). To measure the oxygen isotope composition of each phase, 1–1·5 mg aliquots of 0·5–2·0 mm pale green olivine separates were taken and laser fluorinated. A 25 W CO_2 laser, operating at a wavelength of 10·6 μm, was used to irradiate the samples placed in a 3 mm diameter hole, within a 32-hole nickel sample plug. Pure fluorine desorbed at 290–310°C from hexafluoropotassium-nickelate salt (Asprey, 1976) and stored in a F_2 reservoir, was used as reagent. The O_2 produced during laser fluorination was purified from excess fluorine by means of a KCl trap held at 180°C, and the chlorine was trapped cryogenically. The gas was then transferred to a 13 A° molecular sieve-filled cold finger. Further oxygen gas purification was achieved by desorbing oxygen from the molecular sieve at ∼ −110°C, using a liquid nitrogen–ethanol mixture. In this way the NF compounds were retained on the 13 A° zeolites (Clayton & Mayeda, 1983). The gas was then analysed for oxygen isotope composition using a Finnigan Delta Plus Mass Spectrometer. On each day of analysis, 4–7 aliquots of our laboratory quartz standards were normally analysed, with an average reproducibility of ±0·14‰ (1σ). All samples were analysed in duplicate, with analytical precision of ±0·16‰ (1σ) or better. No data correction is necessary for the results, which are reported in the standard per mil (‰) notation. During the time of the study 11 aliquots of NBS-28 quartz standard were measured, yielding an average value of 9·54 ± 0·17‰ (certified value is 9·60‰). All $\delta^{18}O$ values are relative to VSMOW (Vienna Standard Mean Ocean Water) according to the International Atomic Energy Agency.